Check for updates

The mechanism of eccrine sweat pore plugging by aluminium salts using microfluidics combined with small angle X-ray scattering†

Alice Bretagne,[a] Franck Cotot,[a] Mireille Arnaud-Roux,[a] Michael Sztucki,[b] Bernard Cabane*[c] and Jean-Baptiste Galey ⓘD *[a]

Aluminium salts are widely used to control sweating for personal hygiene purposes. Their mechanism of action as antiperspirants was previously thought to be a superficial plugging of eccrine sweat pores by the aluminium hydroxide gel. Here we present a microfluidic T junction device that mimics sweat ducts, and is designed for the real time study of interactions between sweat and ACH (Aluminium Chloro Hydrate) under conditions that lead to plug formation. We used this device to image and measure the diffusion of aluminium polycationic species in sweat counter flow. We report the results of small angle X-ray scattering experiments performed to determine the structure and composition of the plug, using BSA (Bovine Serum Albumin) as a model of sweat proteins. Our results show that pore occlusion occurs as a result of the aggregation of sweat proteins by aluminium polycations. Mapping of the device shows that this aggregation is initiated in the T junction at the location where the flow of aluminium polycations joins the flow of BSA. The mechanism involves two stages: (1) a nucleation stage in which aggregates of protein and polycations bind to the wall of the sweat duct and form a tenuous membrane, which extends across the junction; (2) a growth stage in which this membrane collects proteins that are carried by hydrodynamic flow in the sweat channel and polycations that diffuse into this channel. These results could open up perspectives to find new antiperspirant agents with an improved efficacy.

Introduction

Sweat

Eccrine sweat glands are widely distributed across the skin in humans, with surface concentrations varying from less than 50 glands per cm^2 in some leg areas to more than 500 glands per cm^2 in the palms of the hands.[1] The major function of eccrine sweat glands is to participate in body core temperature regulation by water evaporation under thermal stress conditions.[2] Eccrine sweat glands have the ability to secrete large amounts of sweat in a pulsatile way depending on the level and type of stimulation.[3,4] The maximum steady state sweat rate during exercise is reported to vary from 0.72 to 3.65 mg cm^{-2} min^{-1} depending on the body area.[1] Inter-individual maximal flow varies

from 4 to 34 μg min^{-1} per gland, corresponding to 0.06 to 0.56 nL s^{-1} per gland.[5]

The structure of eccrine sweat glands consists of a tubule that extends from the skin's surface down through the epidermis to a coiled secretory portion into the lower dermis (Fig. 1).
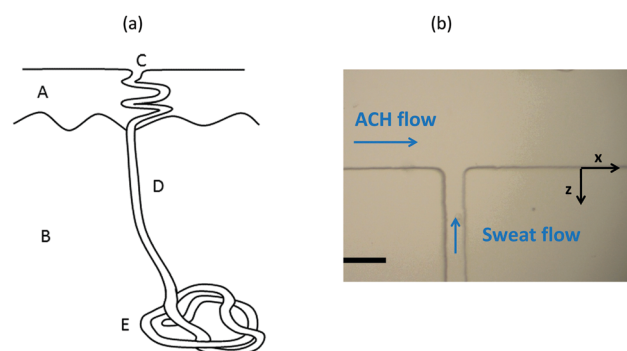
Fig. 1 (a) Schematic drawing of an eccrine sweat gland cross section. A epidermis, B dermis, C sweat pore, D duct, E secretory coil. (b) Photograph of the microfluidic chip with the T junction filled with fluids. Blue arrows indicate flows direction in each channel; bar = 100 μm.

[a] L'Oreal Recherche & Innovation, 1 avenue Eugène Schueller, 93600 Aulnay-sous-Bois, France. E-mail: jbgaley@rd.loreal.com

[b] ESRF – The European Synchrotron, CS 40220, 38043 Grenoble Cedex 9, France

[c] LCMD, CNRS UMR8231, ESPCI, 10 rue Vauquelin, 75231 Paris Cedex 05, France. E-mail: bernard.cabane@espci.fr

† Electronic supplementary information (ESI) available: Video files of optical microscopy imaging and SAXS data. See DOI: 10.1039/c6sm02510b

The intra-epidermal part of the sweat duct, called acrosyringium, has a luminal diameter between 20 and 60 μm.[6] Sweat duct orifices, called ductal pores, have a funnel-like appearance in specific areas such as palm hands, but are generally inconspicuous in most other areas, especially the non-glabrous regions such as axilla, where they are hidden by keratinized cells at the intersection of skin creases.[7]

Sweat collected at the skin surface is mainly composed of water containing sodium chloride and a low concentration of proteins[2,8] as well as low levels of solutes such as potassium, calcium, lactate, urea, bicarbonate, amino-acids and peptides at a pH of 5–7. In the present work, we use either natural sweat or artificial sweat in the form of a solution containing 0.1% BSA (Bovine Serum Albumin) as a model protein. Despite the existence of a myoepithelial layer in the secretory coil, contractility does not seem to play a role in expulsing sweat to the surface. Instead, the function of the myoepithelium is to provide the structural support that permits the generation of the hydrostatic pressure required to overcome the downstream friction and deliver sweat to the skin surface.[9] The intraluminal pressure[10] can rise to 65 kPa when sweat flow exceeds 0.16 nL s^{-1}.

Mimicking sweat pores using a microfluidic device

The size of the sweat pore, 20 to 60 μm in diameter, and the flow rates of sweat, 0.1 to 0.6 nL s^{-1}, led us to consider the use of microfluidics to mimic low Reynolds number hydrodynamic conditions existing in sweat pores at the surface of human skin. We designed a PDMS microfluidic chip to enable in real time a direct observation of the events that take place when an ACH solution gets into contact with the flowing sweat.[11] This device comprises two orthogonal channels with rectangular sections, connected by a T junction (Fig. 1). The ACH "surface channel", which mimics the skin surface, was designed to be large (55 μm high × 400 μm wide) so that it could behave as a reservoir of ACH, whereas the "sweat channel" was 55 μm high × 50 μm wide, thus mimicking sweat pore dimensions. A micro syringe pump delivered fluids through both channels at flow rates in the low nL s^{-1} range (see the Materials and Methods section). Sweat flows were chosen to match or approximate physiological linear velocities. For a 30 μm diameter cylindrical sweat duct flowed with 0.06 nL s^{-1} sweat, the average linear velocity is 21 μm s^{-1}. Hence, we used a flow rate of 0.1 nL s^{-1} in order to get in our device a nearly physiological linear velocity of 36 μm s^{-1}.

Sweat pore plugging by aluminium salts

The microfluidic system described above is well adapted to the study of sweat pore plugging by aluminium salts, which is generally recognized as the basic mechanism for their anti-perspirant action. We used ACH (Aluminium Chloro Hydrate) as a representative antiperspirant aluminium salt. This salt, which is formally $Al_2(OH)_5Cl$, actually yields slightly acidic solutions (pH around 4) that contain complex mixtures of large soluble polycationic aluminium species such as εAl_{13} and Al_{30}, with molecular weights ranging from 1000 to more than 5000 Da.[12] Since these species are known to precipitate as aluminium hydroxide at neutral to basic pH, the plugs have been most

often described to result from the diffusion of such polycations down the acrosyringial part of the sweat duct where they would react with the more alkaline sweat and precipitate as aluminium hydroxide.[13] Several studies have indeed demonstrated the presence of a temporary physical obstruction of the duct.[14–17] This obstruction was believed to be due to the aluminium hydroxide gel associated with mucopolysaccharides.[13] In the case of ACH formulations, the action is reported to be relatively superficial since tape stripping is able to restore normal sweating, *i.e.* that plugs are eliminated by the removal of the first layers of stratum corneum.[13]

Recent progress in understanding the structure–activity relationships of antiperspirant aluminium species has benefited from the structural characterization of these polycations through ^{27}Al NMR, as well as from investigations of their interactions with proteins in solution to form soluble complexes and water insoluble aggregates.[18–20] This behaviour is considered to be similar to the coagulation and flocculation of organic matter by aluminium salts in waste-water treatment.[21] This raises the possibility of an alternative mechanism for plug formation, as the number of ionic groups carried by sweat proteins far exceeds the number of hydroxide ions that can be delivered to the polycations by the sweat. However, no precise self-consistent description of this mechanism at the level of individual sweat duct and under hydrodynamic conditions that mimic normal sweat flow has been proposed yet.

Results

Competition between diffusion and advection

Plug formation by the deposition of reactive species in the vicinity of the duct orifices is related to the ability of these species to enter the sweat duct through diffusive (random) or hydrodynamic (nonrandom) motions. In the T junction, the aluminium polycations that are carried by the flow of ACH solution to the entrance of the sweat channel ($z = 0$) can move into it ($z > 0$) through Brownian diffusion. This diffusion can be described in general terms as the motion of non-interacting species within semi-infinite space. Hence, if there is no flow in the sweat channel, we may calculate the average displacement in the z direction as $z = (2Dt)^{(1/2)}$, where D is the diffusion coefficient of the aluminium polycations, which can be estimated by the Stokes formula. For species of hydrodynamic radius $a = 1$ nm in water ($\eta = 0.001$ Pa s), the calculated diffusion coefficient is $D = 2.2 \times 10^{-10}$ m^2 s^{-1} at $T = 300$ K. We can compute the concentration $n(z, t)$ of these species according to their depth z and the diffusion time t. If the polycations are released at the depth $z = 0$ with an initial concentration n_0, and diffused in the direction $z > 0$, their concentration at depth z is given by Fick's second law:

$$n(z, t) = n_0 \mathrm{erfc}\left(\frac{z}{2\sqrt{Dt}}\right) \qquad (1)$$

On the other hand, if the product is applied during "active sweating", species that enter the channel through Brownian diffusion are caught by a hydrodynamic flow that flushes the
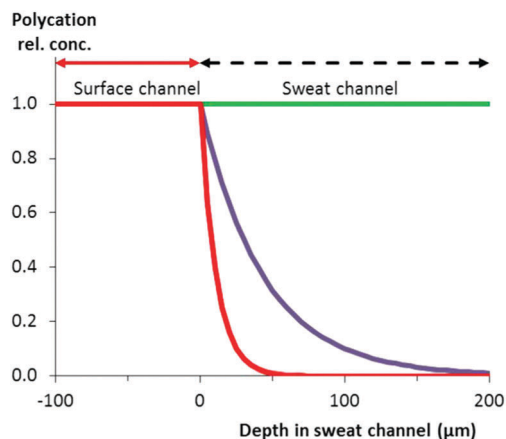
Fig. 2 Steady state relative concentration profiles of polycations diffusing into the sweat channel against a countercurrent of sweat. It is assumed that the flow of the ACH solution maintains a constant concentration of polycations (radius 1 nm) throughout the ACH channel (negative values of depth). Some of these polycations diffuse into the sweat channel (positive values of depth) against the current of sweat, which flows with a velocity of 0 (green), 5 (purple), and 20 (red) μm s^{-1}.

channel, with a displacement proportional to the time, *i.e.* at constant velocity v. At long times (typically a few minutes) the competition between advection and diffusion results in a steady state profile for the concentration of diffusing species. This profile is given by the steady state solution of the advection–diffusion equation with boundaries of the constant polycation concentration at the depth $z = 0$ where the channels merge, and vanishing concentration at very large depths:[22]

$$n(z) = n_0 \exp\left(-\frac{vz}{D}\right) \qquad (2)$$

Fig. 2 illustrates the diffusion of 1 nm polycations in the sweat channel against different sweat flows. According to eqn (2), the polycations diffuse into the sweat channel over a characteristic depth $z_{max} = D/v$ which is 6 μm if the hydrodynamic radius of the polycations is 1 nm, and they remain in the sweat channels for times on the order of 1s before being flushed out.

Moreover, the same approach can be used to demonstrate that macromolecules with low self-diffusion coefficients are flushed out even by sweat flows of low hydrodynamic velocity. This hydrodynamic "self-cleaning" may be particularly efficient in periods of intense sweating, where the hydrodynamic velocity can reach hundreds of μm s^{-1}, in agreement with low efficacy of the antiperspirant applied during the active sweat phase.[13] One may wonder, however, to what extent these predictions may be modified according to the real flow in the sweat channel, for instance if it is of the Poiseuille type, with nearly zero velocity near the walls. In this case, species that remain close to the channel walls could diffuse into the sweat channel even under conditions of intense sweating.

Visual observation of microchannel plugging

The microfluidic set-up produced plugs within the sweat channel using natural eccrine sweat, flowed at 0.1 nL s^{-1} in the sweat

channel and an aqueous solution of ACH 15% (wt%) flowed at 1 nL s^{-1} in the surface channel. The images shown in Fig. 3 (see also Video M1 in the ESI†) illustrate the time-dependent interactions between diffusing aluminium species and sweat components under realistic flow conditions, as they cause the formation of a dense structure that seems to plug the sweat channel. It must be emphasized that ACH 15% is a typical concentration found in common antiperspirant products, corresponding to 50 mM Al$_{30}$ if all polycations were in the form of Al$_{30}$. When sweat flow was maintained for a long time, this structure became progressively denser. Consequently it became a real plug that blocked the sweat flow and was finally ejected.

Similar plugs in terms of shape, thickness and optical density were obtained when natural sweat was replaced by "artificial sweat" containing 0.1% BSA (Fig. S1, ESI†). Artificial sweat we used is an aqueous solution of 0.5% NaCl, 0.1% urea and 0.1% lactic acid, with the pH adjusted to 6.5 using ammonia, as defined by the European Standard EN 1811.[23] Remarkably, the same artificial sweat solution without BSA did not produce any insoluble aggregates or plugs (Fig. S1 (ESI†), left panel). Altogether, these results support the idea that the presence of proteins is essential for plug formation and justify the use of BSA for further investigations.

However, under conditions shown in Fig. 3, it was noticed that plug localization was not reproducible from one experiment to another (plugs were sometimes observed more than 300 μm away from the junction). This behaviour is likely linked to transient regimes occurring when both fluids admix, due to strong differences in Laplace pressures at the fluid surfaces just before the contact of the two menisci. Therefore, a change in channel dimensions was decided in order to minimize transient flows. In this second version, the sweat channel width was enlarged from 50 to 300 μm, with a 120 μm height, whereas the surface channel width was set to 800 μm. These changes did not significantly alter the hydrodynamics of the system but decreased the Laplace pressure at both menisci and hence reduced the impact of transient regimes upon plug localization. With this second version, we used a standard sweat flow of 0.5 nL s^{-1} in the sweat channel corresponding to an average linear velocity of 13.8 μm s^{-1}, in the range of the physiological sweat rate.

This second chip made it possible to get more reproducible plugging behaviours, in terms of density, location and growth
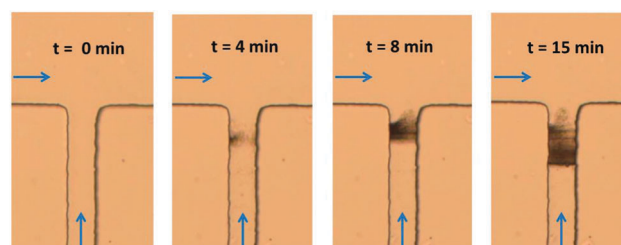

Fig. 3 Typical plugging behaviour observed with the microfluidic chip flowed by 0.1 nL s^{-1} natural eccrine sweat and 1 nL s^{-1} aqueous 15% ACH in the surface channel, corresponding to average linear velocities of 36 and 45 μm s^{-1}, respectively (sweat channel width = 50 μm). Blue arrows represent flow directions in each channel.
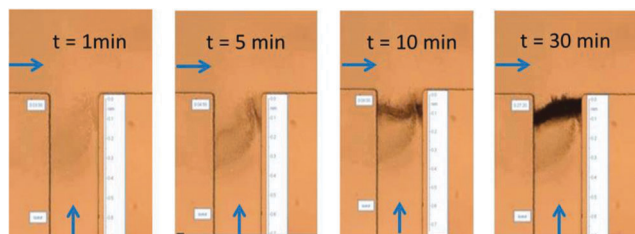
Fig. 4 Typical plugging behaviour observed with a wide channel micro-fluidic chip flowed by 0.5 nL s^{-1} artificial sweat containing 0.1% BSA (15 μM) and 1 nL s^{-1} aqueous 15% ACH in the "surface channel", corresponding to average linear velocities of 13.8 and 10.4 μm s^{-1}, respectively (sweat channel width 300 μm). Blue arrows represent flow directions in each channel.

dynamics, in at least three independent experiments. Typical results are shown in Fig. 4 and in Video M2 (ESI†). This video shows different aggregation dynamics and spatial distributions of dense structures suggesting subtle differences in growth mechanisms revealed by successive growth fronts that could be associated with different polycationic species present in ACH solution. In Video M1 (ESI†) (narrow channels), several parallel growth fronts can be observed perpendicular to the channel axis for early time, whereas for wider channels, the aggregates take a tilted orientation probably determined by hydrodynamic forces applied to them by both flows. Note also the progressive densification of the superficial plug and the dendrite-like structures that grow at late times.

SAXS experiments

In order to gain access to the structure and composition of the plug, *in situ* small angle X-ray scattering experiments were performed. Using instrument ID13 at ESRF, we scanned the T cell with a microfocused beam of X-rays, and we measured the intensity of X-rays scattered at small angles by the solutions that flowed through the T cell. The information was thus both spatially resolved and time resolved. Due to the physical characteristics of the SAXS instrument, we had access only to the median-q part of the scattering, in which the intensities were proportional to the concentrations of the various types of particles, *e.g.* of the various protein + polycation aggregates. This is demonstrated in Fig. S2 and S3 (ESI†), where the scattered intensities from (protein + ACH) aggregates can be rescaled to match the spectrum of BSA between $q = 0.2$ and $q = 3$ nm^{-1}. In this q-range, these spectra differ only by a scale factor, which is the concentration of aggregates.

In a first stage, the scattering from the separated components of the system, *i.e.* the solution of ACH polycations and the solution of BSA macromolecules, was measured (Fig. 5). The spectrum of the ACH solution has a depression at low q followed by a maximum that are characteristic of repelling polyions.[24–27]

From a model for these spatial correlations or approximately from the peak position, we may calculate an average distance between polycations. From their mass concentration and composition, it is then possible to calculate their number concentration and the number of Al atoms per polycation. Thus from the
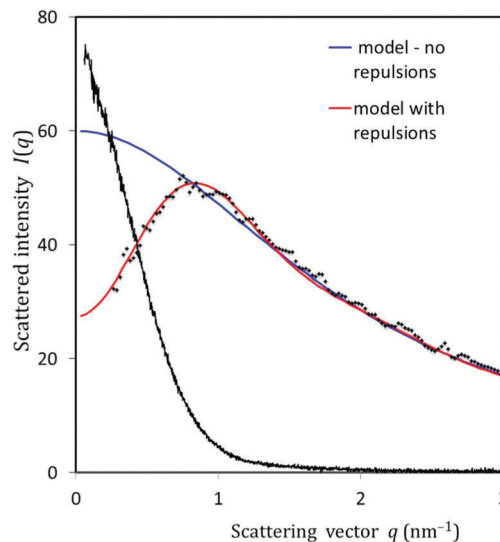

Fig. 5 SAXS spectra of both solutes, each one alone in water. Full black line: spectrum recorded in a 1% BSA solution. Black dots: spectrum recorded in a 1% ACH solution. Blue line: model for branched ACH polymers. Full red line: model for repelling branched ACH polymers. The two solutes produce their main scattering in very different ranges of q, which makes it possible to decompose the scattering from the T junction into the contributions of the components.

spectrum shown in Fig. 5, we calculate that each polycation in a 1% ACH solution contains, on average, 25 Aluminium atoms (see also Fig. S5, ESI†). Conversely, the spectrum of the BSA macromolecules has a maximum of intensity at low q, as expected for macromolecules that have only weak repulsions with each other. Since the two solutes produce their main scattering in very different ranges of q, it is possible to decompose the scattering from the T junction into the contributions of the components.

In a second stage, in order to determine the microstructure of the plug, we scanned a T-junction with 500 × 500 μm channels in front of a micro-focused X ray beam of 2 μm × 3 μm (vertical × horizontal) size. The experiments were conducted as described above, but using faster flow rates, a 10 nL s^{-1} flow rate of artificial sweat at pH6.5 containing 1% BSA (150 μM), and a 50 nL s^{-1} flow rate of a 1% ACH solution (corresponding to 3 mM Al$_{30}$ if all polycations were in the form of Al$_{30}$). This corresponds to hydrodynamic velocities of 40 μm s^{-1} for the artificial sweat and according to eqn (1) and (2) to the penetration depth of less than 10 μm. The entire T-junction was mapped in a matrix of 10 × 10 ccd images which were 50 μm spaced in the horizontal direction and 100 μm spaced in the vertical direction (see Fig. 6). Scans collected along a column within the sweat channel indicated how polycations diffused through thermal agitation into the sweat channel and how they produced protein aggregates when they met proteins that were carried by the flow.

Fig. 6b presents the intensities scattered at $q \rightarrow 0$ from the scattering structures located in column E, in the middle of the sweat channel. At early times (6 min), cells E8, E9, E10 (inside sweat channel) gave spectra that were similar to the high-q part of the scattering from a BSA solution (Fig. S2, ESI†).
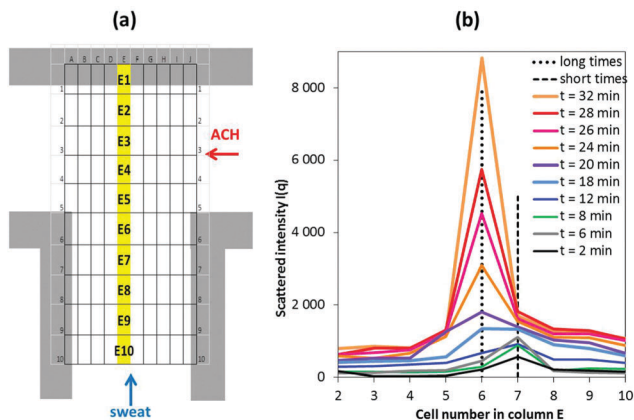
(a)

(b)

Fig. 6 (a) Schematic representation of 10 × 10 scanned area (cell size of 50 μm width × 100 μm height) of a T-junction cell with 500 × 500 μm channels. Arrows show the direction of flows of artificial sweat (blue) and ACH (red). (b) Profiles of intensity scattered at low q values (arbitrary unit) by cells located along the central column, highlighted in yellow. Notice the weak peak of intensity at cell E7 for early flow times. Notice the sudden jump in the peak position at $t = 12$ min, and the very fast rise in intensity that follows.

Conversely, cells E2, E3 and E4, within the surface channel, gave spectra characteristic of aluminium polycations. Only cell E7 gave relatively high intensities at low q values, signalling the presence of aggregates that probably originate from BSA coming into contact with polycations that have diffused into the sweat channel. Thus, at short times, the scattering shows BSA within the sweat channel, polycations within the surface channel, and aggregates only at the location of cell E7. The concentration of aggregated BSA that has accumulated in cells E10, E9, E8 and E7 was respectively 0.04, 0.12, 0.25 and 1.5 times that of the BSA solution (S2, ESI†). These concentrations indicate that the early deposit was a tenuous network of BSA aggregates.

At later times (12 to 32 min), the location of the maximum intensity was shifted by one cell (E7 to E6) toward the surface channel, and the magnitude of this scattered intensity increased sharply (Fig. 6b), whereas at all other cells the intensity kept growing at a slow pace. These features reflect the formation of a gel membrane at a location determined by the balance of hydrodynamic forces exerted by both fluids. It can be argued that, as the gel membrane became large enough, it took an orientation that was determined by hydrodynamic forces applied to it by both flows (Fig. S4, ESI†). In this new position, it was closer to the flux of polycations, and consequently it grew faster.

The SAXS spectra also reveal the presence of strong concentration gradients within the plug. Cells E10 to E6 gave spectra that were characteristic of protein aggregates: at high q, these spectra can be scaled to match the BSA spectrum, and the scaling coefficients yield the concentration of aggregated BSA along column E (Fig. S2 and S3, ESI†).

At long times (32 min), the concentration of aggregated BSA that had accumulated in cells E10, E9, E8, E7 and E6 was respectively 1.9, 2.5, 2.7, 3.8 and 28 times that of the BSA solution (S3, ESI†). These concentrations indicate that the fully formed plug was a dense and thin membrane made of BSA aggregated by
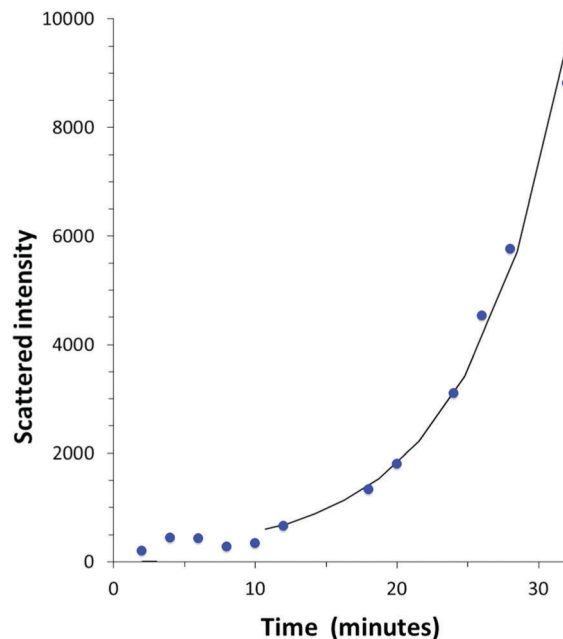

Fig. 7 Scattered intensity at low q value ($q = 0.334$ nm^{-1}) from cell E6 (arbitrary units) as a function of time after opening the flow of polycations and artificial sweat, showing exponential growth starting after nucleation phase until plug ejection. This exponential growth is consistent with eqn (3) in the Discussion section.

ACH polycations. The evidence for the formation of a membrane is (a) the peak of scattered intensity that grows in the exploration of a column and (b) the narrow width of this peak (100 μm as upper bound given by the scanning interval). These features indicate that the aggregation takes place at a single depth, as in the formation of a membrane. Fig. 7 shows the complete variation with time of the intensity scattered at low q by cell E6. For the first 10 minutes it shows the nucleation stage, and for later times it displays an exponential growth regime until its expulsion.

At very long times, all these plugs were ejected from the sweat channel, and the scattering returned to the sum of that of free BSA macromolecules plus that of free polycations (Fig. S6, ESI†). This was expected, since the pumps were operated at a constant flow rate, and the hydraulic pressure increased in the sweat channel as the plug collected more proteins, until it exceeded the ejection pressure.

Discussion

In this section we aim at answering two questions:

– Does the microfluidic device described above provide an adequate representation of the biological system?

– Can we use the results obtained with this device to determine the mechanism of sweat pore plugging by aluminium polycations?

Does the microfluidic device provide an adequate representation of the biological system?

A first issue is whether the T junction made of a sweat channel connected to a surface channel matches *in vivo* conditions,

where sweat duct outlets are opened to the skin surface. Considering the natural wetness of the armpit region and the film resulting from antiperspirant formula applications, it can reasonably be assumed that a concentrated ACH film of a few hundreds of microns is present at the skin surface following application onto armpit, which is comparable to the width of the surface channel, both being comparable to an infinite ACH reservoir.

Furthermore, our device takes into account both diffusion and hydrodynamic flow, and therefore reproduces conditions which are much closer to physiological situation than bulk studies that are usually performed to investigate the interaction of ACH with proteins.[18,28] In addition, our system is compatible with SAXS investigations to allow dynamic *in situ* studies under flowing conditions as recently described for other systems.[29,30] In contrast, other microfluidic devices mimicking sweat flow have been reported, but they were designed to provide a model for skin surface perspiration and biomarker sensing[31,32] and not to monitor sweat pore plugging. To our knowledge, our work allows for the first time a direct real time observation of the formation of plugs inside a channel mimicking a sweat duct.

Another question is whether the device reproduces adequately the phenomena that take place within the sweat duct. In this respect, the model presented here uses realistic fluids, either sweat collected from human volunteers or artificial sweat, and controlled physiological flows. A further point concerns the use of a constant sweat flow rate whereas it is known that physiological sweat generation is pulsatile. A continuous flow was chosen to facilitate experimental work, but the question of pulsatile flow is addressed at the end of the Discussion. Furthermore, it must be emphasized that, in our experiments we used sweat flows giving rise to average linear velocities in the range of physiological values. Therefore, we think that these conditions are well suited to model sweat pore plugging, the wider channels being better adapted to SAXS experiments.

Moreover, PDMS surfaces are known to adsorb proteins[33] and therefore, it is likely that channel surfaces are fully coated with sweat proteins, thereby mimicking sweat duct walls. It may be argued that sweat duct walls are not only composed of proteins, but close to the skin surface, duct walls are considered to be similar to stratum corneum composition, *i.e.* keratinized flat dead cells. At a greater depth, acrosyringium consists of living epithelial cells mainly composed of lipid bilayers embedded with membrane proteins. But, like all epithelia, these living cells are covered and protected by a layer of glycoproteins of the mucin family. So it is reasonable to consider aluminium polycation interactions with sweat duct channels through their interaction with surface proteins. On the other hand, although PDMS is probably "smoother" than the acrosyringium surface, the presence of weakly bound proteins on PDMS is apparently sufficient to allow nucleation at the wall surface, as observed in images shown in Fig. 3 and 4.

The next issue is whether a 0.1% BSA solution is fully appropriate as a sweat model. Human sweat collected in the axillary region contains a variety of peptides and proteins at low concentrations, including serum albumin,[2] which is the human homolog of BSA. The choice of BSA as a single macromolecular solute is a classic choice, which has been widely made to study nonspecific interactions of polycations with proteins.[18,34–36] Then there is the choice of the BSA concentration, which was made as follows. The total concentration of proteins and peptides in sweat is in the range of 0.05–0.08 g L^{-1}, lower by one order of magnitude compared to the BSA concentration of experiments presented in Fig. 4 and S1 (ESI†). We chose the 0.1% BSA solution because it produced plugs easily and repeatedly in our set-up regardless of the concentrations and types of polycationic species, which suggests a robust and common mechanism (data not shown). Besides, no aggregation was observed with solutions of much lower BSA concentration (0.01%, data not shown) during the time of our experiments (30 min), indicating that proteins naturally present in sweat are actually more reactive than BSA.

The numbers of negative charges on proteins are of course of paramount importance for the electrostatic interactions with polycations such as ε-Al$_{13}$ and Al$_{30}$, which carry 8 and 18 positive charges, respectively.[12] BSA, which has an isoelectric point at 4.7, carries an inhomogeneous distribution of negative charges on its surface thanks to a large number of glutamate and aspartate residues, with a formal net charge of -13 at pH 7.[37] Its molecular weight (66 kDa) is somewhat higher than that of most sweat proteins, but not out of the range. As a comparison, the main sweat protein, Apolipoprotein D, with a molecular weight of 26 kDa (in the glycosylated form)[38] has an isoelectric point of 5. We can speculate that the reactivity of the different proteins naturally present in sweat with aluminium polycations might differ slightly compared to BSA, according to their charge distribution, but is likely based on similar non-specific interactions of electrical charges.

What is the mechanism for plug formation?

Our observations show that macroscopic aggregation does not start unless proteins are present, and therefore that it involves reactions of aluminium polycations with sweat proteins. The first aggregates resulting from the interaction of ε-Al$_{13}$ and Al$_{30}$ with BSA have been estimated to have an average particle size in the range of 10–11 nm by Dynamic Light Scattering under non flowing conditions.[18] Here, we show that these reactions further produce macroscopic aggregates that are found in the sweat channel, at a short distance from the skin surface where the sweat and ACH flows meet. This is consistent with the idea that ACH polycations diffuse upstream into the sweat channel until they meet proteins. Then, BSA-polycation aggregates are carried away by the flow unless they connect directly or indirectly to a wall.

The results from SAXS experiments show that the aggregation proceeds in two stages. At short times (6 min), the scattering from cells located in the sweat channel away from the junction (= cells E10, E9, E8) is similar to that of the BSA solution, except at $q \to 0$ where it has higher intensities and a steeper slope, reflecting the presence of a few large BSA-polycation aggregates. Cell E7 is the only cell that has a substantial concentration of these aggregates (1.5 times that of the BSA solution), due to its location at a short

distance from the source of polycations. We can estimate the efficiency with which these early aggregates capture free proteins from the counter flow. This evaluation is a mass balance calculation applied to a 100 μm thick slice located in the sweat channel, at the depth where the SAXS experiment found a thin gel membrane. This mass balance does not depend on the slice thickness, as long as this thickness is much larger than the gel membrane thickness, and therefore counts all the proteins captured by the membrane. The total mass M_{sweat} of proteins that have been brought to the plug by the sweat flow during Δt equals the mass M_{bound} of proteins that have bound into the plug during Δt plus the mass of proteins M_{out} that have crossed the plug during Δt.

$$M_{\text{sweat}} = M_{\text{bound}} + M_{\text{out}} \tag{3}$$

We define the capture efficiency as the ratio $M_{\text{bound}}/M_{\text{sweat}}$, and we calculate this fraction from experimental quantities. Firstly, we use the protein concentration C of the incoming sweat (which is constant) and the flow rate F (which is also constant) to calculate the total mass of proteins:

$$M_{\text{sweat}} = FC\Delta t \tag{4}$$

Next we use the intensity of X rays scattered by the deposit at the end of interval Δt to calculate the total mass of proteins M_{slice} that are in the slice, bound or not bound, through a comparison with the intensity scattered by an equal volume of protein solution:

$$M_{\text{slice}}/M_{\text{solution}} = I_{\text{slice}}/I_{\text{solution}} \tag{5}$$

The slice contains proteins that are bound to the plug and free proteins:

$$M_{\text{slice}} = M_{\text{bound}} + M_{\text{solution}} \text{ (sum rule for the slice)} \tag{6}$$

At this point we make the assumption that the concentration of free proteins crossing the plug is equal to the concentration of incoming proteins, $C_{\text{solution}} = C$. This is validated by the result of this calculation.

$$M_{\text{solution}} = V_{\text{slice}}C \tag{7}$$

Hence we may calculate:

$$M_{\text{bound}} = M_{\text{slice}} - M_{\text{solution}} = M_{\text{solution}}\{I_{\text{slice}}/I_{\text{solution}} - 1\} \tag{8}$$

The capture efficiency of the plug is obtained as:

$$M_{\text{bound}}/M_{\text{sweat}} = \{V_{\text{slice}}/F\Delta t\}\{I_{\text{slice}}/I_{\text{solution}} - 1\} \tag{9}$$

With a hydrodynamic flux $F = 10$ nL s^{-1} = 0.01 mm^3 s^{-1} and $\Delta t = 360$ s, the amount $F\Delta t$ of model sweat that has flown through the junction during Δt amounts to = 3.6 mm^3. In comparison, the volume V_{slice} of the slice in which the deposit was found is 100 × 500 × 500 μm = 0.025 mm^3. Hence the volume of sweat that has flown through the deposit is 3600/25 = 144 times the volume V_{slice} of the slice. The excess intensity measured at the end of Δt is $\{I_{\text{slice}}/I_{\text{solution}} - 1\}$ = 1.5, which yields a capture efficiency $M_{\text{bound}}/M_{\text{sweat}}$ = 1.5/144 = 1/100 for the early plug, which means

that a protein going through the T junction has only one chance out of nearly 100 of being captured by the growing membrane. This low value of the capture efficiency of the membrane indicates that it is very thin and highly porous, so that most sweat proteins can navigate through its pores. It also suggests that most proteins in this structure have not been fully aggregated. In this case, all the proteins that have been caught are still available for catching other free proteins or aggregates. At long times (1920 s) the volume of sweat that has flown through the deposit is $F\Delta t = 0.01 \times 1920 = 19.2$ mm^3, i.e. 768 times the volume of the slice. The excess intensity is $I_{\text{slice}}/I_{\text{solution}} = 26.5$, hence the capture efficiency is 26.5/768 = 1/30 for the later stage. These low values or the capture efficiency validate the approximation $C_{\text{solution}} = C$ made in eqn (7), i.e. the concentration of free proteins crossing the plug is nearly the protein concentration of the incoming sweat.

In summary, the plug formation mechanism appears to follow a nucleation and growth scheme, based on the following experimental results:

– At early times, the formation of a thin gel membrane is demonstrated by the narrow peak (Fig. 6b) that grows in the profile of a column oriented across the junction and along the sweat flow. Remarkably, the height of this peak stagnates during the first few minutes (Fig. 7) until a random event (the switch in depth from E7 to E6 at time = 12 minutes, Fig. 6b) kicks it into a location with a higher capture efficiency (Fig. 7). This is characteristic of a nucleation process.

– At later times, the higher capture efficiency and the exponential growth that result (Fig. 7) indicate that the evolution of the membrane into a real plug is a growth process in which every captured protein becomes a center of new growth. As a matter of fact, if we consider an aggregate containing n_{p} proteins and n_{c} polycations, the number of proteins this aggregate captures per unit time, dn_{p}/dt, is proportional to the number n_{p} of proteins that have been caught already:

$$dn_{\text{p}}/dt = Kn_{\text{p}} \text{ or } n_{\text{p}} = (n_{\text{p}})_0 \exp(Kt) \tag{10}$$

where $K = 0.0024$ s^{-1} is the rate constant that we can obtain from fitting the data of Fig. 7 to an exponential kinetic law. This value can be compared to the advection time for crossing the slice multiplied by the capture efficiency.

This process differs from ordinary growth regimes by the fact that the incoming proteins are continuously fuelled by the flow of new sweat rather than fully consumed by random motions within a still fluid. Consequently, the growth of the plug is unavoidable when sweat flows.

Fig. 8 presents a simple schematic representation of this overall mechanism. The left panel represents the building of a tenuous network after aggregates have anchored to the wall, and the right panel depicts the plug formed by subsequent accumulation over this network leading to a denser clogging structure.

Such 2-dimensional image projections are useful in order to visualize the aggregation mechanism in counter flow. However it is useful to keep in mind that aggregates in 3-dimensions are more porous than they would appear in a 2-dimensional image.
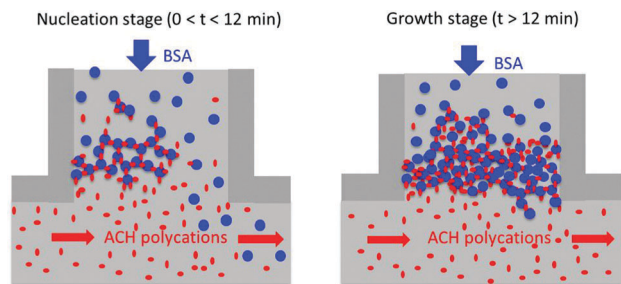
Fig. 8 A schematic, two-dimensional image of the initial membrane (left) and of a fully-grown plug (right).

Therefore, they may let a fast current of sweat flow through one pore located on one side of a plug.

Another interesting situation to consider is a two stage condition, first in the absence of sweat flow and then with a positive sweat flow, which is relevant for physiological pulsatile sweating. In this case, the protein–polycation aggregates would first grow at a slow pace through Brownian encounters at a constant protein concentration and then more quickly as new proteins are supplied continuously to the plug when the flow is turned on as illustrated in Fig. 9.

In the absence of sweat flow, the proteins and polycations encounter each other only through their own Brownian motions according to the Smoluchowski equation:

$$\mathrm{d}n_{\mathrm{p}}/\mathrm{d}t = -K_{\mathrm{s}}(n_{\mathrm{p}})^2 \text{ or } 1/n_{\mathrm{p}} = (1/n_{\mathrm{p}})_0 + K_{\mathrm{s}}t \qquad (11)$$

where K_{s} is the Smoluchowski constant (1.1×10^{-17} m^3 s^{-1} at 25 °C).[39] With an initial number density of 1.8×10^{18} aggregating proteins per m^3, eqn (11) leads to a fast initial growth
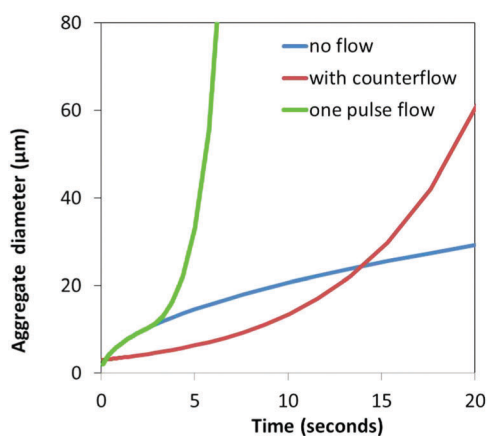

Fig. 9 Growth laws of the protein–polycation aggregates calculated according to the competition of diffusion and advection in the sweat channel. Sweat proteins of diameter 3 nm encounter and bind oppositely charged aluminium polycations, and these aggregates encounter and bind to each other. Blue line: no sweat flow, the average radius of the aggregates as a function of time was calculated through the kinetic Smoluchowski eqn (11). Brown line: continuous sweat counter flow of 10 nL s^{-1} (average linear velocity of 40 μm s^{-1}), the average radius of aggregates was calculated using eqn (10). Green line: no flow in a first 2.5 s stage (eqn (11)), then positive sweat flow of 10 nL s^{-1} turned on at t = 2.5 s until t = 20 s (eqn (10)).

(the initial size doubles in the first 0.4 s), but a much slower growth at longer times (the average number of particles per aggregate grows linearly with time, consequently the radius of the aggregates grows only as the cube root of time: it takes 1.6 s for the average radius to double again).

Therefore, if sweat flow is applied after a first stage without flow, the mass of protein captured by the plug would grow faster than if the flow had been applied continuously for the same period of time. Hence, a pulsatile flow could contribute to build the plug faster than a continuous flow.

Furthermore, we can also speculate that the intriguing local spatial aggregation dynamics observed in Movies M1 and M2 (ESI†) are related to such phenomena, since local hydrodynamic modifications could induce different growth regimes on small scales. However, other SAXS studies, as well as numerical simulations will be necessary to interpret these specific local growth dynamics.

Conclusion

In conclusion, our results suggest that pore plugging occurs as a result of the aggregation of proteins by aluminium polycations at specific locations in the sweat channel. These processes take place where both hydrodynamic and diffusive flows achieve sufficient concentrations of proteins and polycations with balanced positive and negative electrical charges. This deposit grows exponentially by capturing species provided by the flow and becomes a denser obstacle to a free flow. In spite of their low concentrations, sweat proteins are essential to build this plug. ACH aggregation by sweat proteins at the entrance of the sweat pore, associated with hydrodynamic "self-cleaning" described above, may also be seen as an argument in support of a very limited capacity of aluminium salts to disseminate deeply into sweat channels. Altogether, these results could help to find new antiperspirants active with improved efficacy based on the size and charge of the reactive species found in the present work and on their ability to react with sweat proteins and proteins present at the surface of sweat pores.

Materials and methods

Materials

Lactic acid, urea, sodium chloride and bovine serum albumin were purchased from Sigma-Aldrich.

Aluminium Chlorohydrate (ACH) was purchased from Summit Reheis (reference ACH-321). Artificial sweat used has the following composition: 0.5% (w/w) NaCl, 0.1% lactic acid, 0.1% urea and 0.1% BSA at pH 6.5 (adjusted with ammonia). Natural human sweat was collected from the armpit of volunteers after a sauna session and immediately frozen.

Microfluidic device

PDMS chips were manufactured using soft lithographic techniques, as previously reported.[40] Briefly, they were made by casting a PDMS pre-polymer against a negative pattern developed in SU-8

that had been spin-coated on silicon wafers. A mixture of an elastomer base and a curing agent (10 : 1 ratio w/w) was degassed to remove any residual air bubbles and poured on SU-8 relief patterns to achieve a device thickness of 3–5 mm. PDMS was thermally cured at 70 °C for 2 hours. After release, PDMS structures were irreversibly bonded to glass coverslips using plasma oxidation. Gastight syringes (Hamilton) were fitted to 500 μm inner diameter PEEK (poly-ether-ether-ketone) tubing and controlled using microsyringe pumps (Nemeysis). A 20× objective lens mounted on a Zeiss microscope equipped with a white light source was used for all of the experiments. Syringes were filled with sweat and with an aqueous solution of ACH at various concentrations. Experiments consisted in carefully injecting both sweat and ACH solutions into initially empty channels up to the apparition of the meniscus in both channels in the field of view separated by 50–100 μm from each other. Images were then recorded for 30 min every 15 s starting when both menisci get into contact.

Small angle X-ray scattering

SAXS data were acquired (info: 14/05/2014) at the micro- and nano-diffraction beamline ID13 at the European Synchrotron Facility (ESRF), Grenoble, France. The beam size was 2 μm × 3 μm (in horizontal and vertical direction, respectively). The X-ray energy was 13.0 keV, corresponding to a wavelength of 0.954 Å. The scattered intensity was registered using a FReLoN ccd detector located at 15.3 cm from the sample resulting in an accessible q range from 0.1 to 1.5 nm^{-1} where q is the scattering vector equal to $(4\pi/\lambda)\sin(\theta/2)$, θ being the scattering angle. The resulting 2D data were corrected for detector artifacts and azimuthally averaged to 1D scattering profiles. All measurements were carried out at room temperature using a T-junction cell which was aligned perpendicular to the beam. In order to reduce the scattering background, mica windows (100 μm thick) were inserted into the two glass plates of the T-junction cell which were separated by a 0.5 mm silicon elastomer spacer fitted with clamping clips and connected to a 500 μm polyether ether ketone (PEEK) tubing. During the filling phase, the air bubbles were removed by successive flow modifications.

Acknowledgements

References

1 N. A. S. Taylor and C. A. Machado-Moreira, Regional variations in transepidermal water loss, eccrine sweat gland density, sweat secretion rates and electrolyte composition in resting and exercising humans, *Extrem. Physiol. Med.*, 2013, **2**, 1–29.

2 K. Sato, W. H. Kang, K. Saga and K. T. Sato, Biology of sweat glands and their disorders. I. Normal sweat gland function, *J. Am. Acad. Dermatol.*, 1989, **20**, 537–563.

3 M. Harker, Psychological sweating: a systematic review focused on aetiology and cutaneous response, *Skin Pharmacol. Physiol.*, 2013, **26**, 92–100.

4 H. Murota, S. Matsui, E. Ono, A. Kijima, J. Kikuta, M. Ishii and I. Katayama, Sweat, the driving force behind normal skin: an emerging perspective on functional biology and regulatory mechanisms, *J. Dermatol. Sci.*, 2015, **77**, 3–10.

5 K. Sato and R. L. Dobson, Regional and individual variations in the function of the human eccrine sweat gland, *J. Invest. Dermatol.*, 1970, **54**, 443–449.

6 K. Wilke, A. Martin, L. Terstegen and S. S. Biel, A short history of sweat gland biology, *Int. J. Cosmet. Sci.*, 2007, **29**, 169–179.

7 C. Johnson, R. Dawber and S. Schuster, Surface appearance of the eccrine sweat duct by scanning electron microscopy, *Br. J. Dermatol.*, 1970, **83**, 655–660.

8 P. M. Quinton, H. Y. Elder, D. McEwan Jenkinson and D. L. Bovell, Structure and function of human sweat glands, in *Antiperspirants and Deodorants*, ed. K. Laden, Marcel Dekker, New York, 1999, pp. 17–57.

9 K. Sato, A. Nishiyama and M. Kobayashi, Mechanical properties and functions of the myoepithelium in the eccrine sweat gland, *Am. J. Physiol.*, 1979, **237**, 177–184.

10 U. Schultz, Micropuncture studies of the sweat formation in cystic fibrosis patients, *J. Clin. Invest.*, 1969, **48**, 1470–1477.

11 F. Baltenneck, J. B. Galey, M. Dailly, A. Colonna and F. Monti, *Système microfluidique d'évaluation de l'efficacité d'un produit anti-transpirant et procédé associé*, *Patent appl.*, WO2014/170174, 2014.

12 W. H. Casey, Large aqueous aluminium hydroxide molecules, *Chem. Rev.*, 2006, **106**, 1–16.

13 H. H. Reller and W. L. Luedders, Pharmacologic and toxicologic effects of topically applied agents on the eccrine sweat glands, in *Advances in Modern Toxicology*, ed. F. N. Marzulli and H. I. Maibach, Dermatotoxicology and Pharmacology, John Wiley and Sons, New York, 1977, vol. 4, pp. 1–54.

14 E. Hözle and A. M. Kligman, Mechanism of antiperspirant action of aluminium salts, *J. Soc. Cosmet. Chem.*, 1979, **30**, 279–295.

15 R. P. Quatrale, D. W. Coble, K. L. Stoner and C. B. Felger, The mechanism of antiperspirant action by aluminiums salts, II Histological observations of human eccrine sweat glands inhibited by aluminium chlorohydrate, *J. Soc. Cosmet. Chem.*, 1981, **32**, 107–136.

16 T. Yanagishita, Y. Tamada, Y. Ohshima, K. Ito, Y. Akita and D. Watanabe, Histological localization of aluminium in topical aluminium chloride treatment for palmar hyperhidrosis, *J. Dermatol. Sci.*, 2012, **67**, 69–71.

17 X. Chen, P. Gasecka, F. Formanek, J. B. Galey and H. Rigneault, *In vivo* single human sweat gland activity monitoring using

coherent anti-Stokes Raman scattering and two-photon excited auto-fluorescence microscopy, *British J. Dermatol.*, 2016, **174**, 803–812.

18 O. Deschaume, K. L. Shafran and C. C. Perry, Interactions of Bovine Serum Albumin with aluminium polyoxocations and aluminium hydroxide, *Langmuir*, 2006, **22**, 10078–10088.

19 S. Yuan, J. Vaughn, I. Pappas, M. Fitzgerald, J. G. Masters and L. Pan, Optimal aluminium/zirconium: Protein interactions for predicting antiperspirant efficacy using zeta potential measurements, *J. Cosmet. Sci.*, 2015, **66**, 95–111.

20 B. L. Phillips, J. S. Vaughn, S. Smart and L. Pan, Characterization of Al_{30} in commercial poly-aluminium chlorohydrate by solid-state ^{27}Al NMR spectroscopy, *J. Colloid Interface Sci.*, 2016, **476**, 230–239.

21 J. K. Edzwald, Coagulation in drinking water treatment – particles, organics and coagulants, *Water Sci. Technol.*, 1993, **27**, 21–35.

22 Dartmouth engineering course, chapter 2 – diffusion, Section 2.8: Combination of advection and diffusion, page 69 available on the web at: http://www.engineering.dartmouth.edu/~d30345d/courses/.../chapter2.pdf.

23 C. J. Harvey, R. F. LeBouf and A. B. Stefaniak, Formulation and stability of a novel artificial human sweat under conditions of storage and use, *Toxicol. In Vitro*, 2010, **24**, 1790–1796.

24 M. Nierlich, C. E. Williams, F. Boué, J. P. Cotton, M. Daoud, F. Farnoux, G. Jannink, C. Picot, M. Moan, C. Wolff, M. Rinaudo and P. G. de Gennes, Small angle neutron scattering by semi-dilute solutions of polyelectrolyte, *J. Phys.*, 1979, **40**, 701–704.

25 W. B. Russel, D. A. Saville and W. R. Schowalter, *Colloïdal dispersions*, Cambridge University Press, 1979.

26 J. B. Hayter and J. Penfold, An Analytic Structure Factor for Macroion Solutions, *Mol. Phys.*, 1981, **42**, 109–118.

27 J. Chang, P. Lesieur, M. Delsanti, L. Belloni, C. Bonnet-Gonnet and B. Cabane, Structural and Thermodynamic Properties of Charged Silica Dispersions, *J. Phys. Chem.*, 1995, **99**, 15993–16001.

28 O. Deschaume, A. Fournier, K. L. Shafran and C. C. Perry, Interactions of aluminium hydrolytic species with biomolecules, *New J. Chem.*, 2008, **32**, 1346–1353.

29 S. With, M. Trebbin, C. B. Bartz, C. Neuber, M. Dulle, S. Yu, S. V. Roth, H. W. Schmidt and S. Förster, Fast diffusion-limited lyotropic phase transitions studied *in situ* using continuous flow microfluidics/microfocus-SAXS, *Langmuir*, 2014, **30**, 12494–12502.

30 H. P. Martin, N. J. Brooks, J. M. Seddon, P. F. Luckham, N. J. Terrill, A. J. Kowalski and J. T. Cabral, Microfluidic processing of concentrated surfactant mixtures: online SAXS, microscopy and rheology, *Soft Matter*, 2016, **12**, 1750–1758.

31 L. Hou, J. Hagen, X. Wang, I. Papautsky, R. Naik, N. Kelley-Loughnane and J. Heinkenfeld, Artificial microfluidic skin for *in vitro* perspiration simulation and testing, *Lab Chip*, 2013, **13**, 1868–1875.

32 Z. Sonner, E. Wilder, J. Heikenfeld, G. Kasting, F. Beyette, D. Swaile, F. Sherman, J. Joyce, J. Hagen, N. Kelley-Loughnane and R. Naik, The microfluidics of the eccrine sweat gland, including biomarker partitioning, transport and biosensing implications, *Biomicrofluidics*, 2015, **9**, 31301–31319.

33 W. Schrott, Z. Slouka, P. Cervenka, J. Ston, M. Nebyla, M. Pribyl and D. Snita, Study on surface properties of PDMS microfluidic chips treated with albumin, *Biomicrofluidics*, 2009, **3**, 044101.

34 Y. X. Yan, H. B. Yao, S. E. Smart, L. B. Mao, W. Hu, S. Yuan, L. Du-Thumm, J. G. Masters, S. H. Yu and L. Pan, Ultrathin hybrid films of polyoxohydroxy clusters and proteins: layer-by-layer assembly and their optical and mechanical properties, *Langmuir*, 2014, **30**, 5248–5255.

35 K. Rezwan, L. P. L. Meier and L. J. Gauckler, A Prediction Method for the Isoelectric Point of Binary Protein Mixtures of Bovine Serum Albumin and Lysozyme Adsorbed on Colloidal Titania and Alumina Particles, *Langmuir*, 2005, **21**, 3493–3497.

36 R. H. Al-Shakhshir, F. E. Regnier, J. L. White and S. L. Hem, Contribution of electrostatic and hydrophobic interactions to the adsorption of proteins by aluminium-containing adjuvants, *Vaccine*, 1995, **13**, 41–44.

37 L. R. S. Barbosa, M. G. Ortore, F. Spinozzi, P. Mariani, S. Bernstorff and R. Itri, The importance of protein–protein interactions on the pH-induced conformational changes of bovine serum albumin: a Small-Angle X-Ray Scattering Study, *Biophys. J.*, 2010, **98**, 147–157.

38 C. Zeng, A. Spielman, B. R. Vowels, J. J. Leyden, K. Biemann and G. Preti, A human axillary odorant is carried by apolipoprotein D, *Proc. Natl. Acad. Sci. U. S. A.*, 1996, **93**, 6626–6630.

39 D. Fennel Evans and H. Wennerstrom, *The Colloidal Domain: Where Physics, Chemistry, Biology, and Technology Meet*, Wiley-VCH, 2nd edn, 1999.

40 J. C. McDonald and G. M. Whitesides, Poly(dimethylsiloxane) as a material for fabricating microfluidic devices, *Acc. Chem. Res.*, 2002, **35**, 491–499.

Mechanism of eccrine sweat pore plugging by aluminium salts using microfluidics combined with Small Angle X-ray Scattering

Alice Bretagne, Franck Cotot, Mireille Arnaud-Roux, Michael Sztucki, Bernard Cabane and Jean-Baptiste Galey

Supplementary Information

1) Effect of BSA on ACH-induced plugging of microfluidic channels flowed with artificial sweat.

Figure SI-1 illustrates the key role of proteins in plug formation. Artificial sweat solution without BSA did not produce any insoluble aggregates or plugs. Note that the right hand panels of Fig. SI-1 and Fig. 3 show plugs that are similar in their overall shape, thickness and optical density.
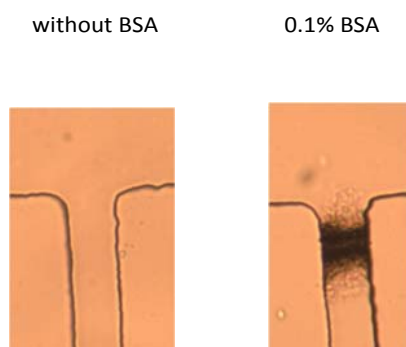
without BSA	0.1% BSA

Figure SI-1: Aggregation plugs or absence of plug observed after 15 min with channels flowed by 0.1 nL.s^{-1} artificial sweat with or without BSA and 1 nL.s^{-1} aqueous 15% ACH in surface channel, corresponding to average linear velocities of 36 and 45 μm.s^{-1}, respectively (sweat channel width = 50 μm). Artificial sweat used contained 0.5% (w/w) NaCl, 0.1% lactic acid, 0.1% urea at pH 6.5 (adjusted with ammonia) with or without 0.1% BSA

2) Additional SAXS data

Figures SI-2 and SI-3 present a quantitative determination of the concentrations of BSA in each matrix element of the T junction cell described in Figure 6. This information is provided by the calculation of the integral of the scattering, which yields the total fluctuation of electronic density in the irradiated volume. Thus, for each matrix element in the cell near the junction, and at every time, we determined a rescaling coefficient as the ratio of the measured integral to the integral measured in a matrix element of the sweat channel far from the junction, in a place where the channel contained only the pure BSA solution. The expression of the integral of the intensity over all scattering vectors, also called the invariant, is :

$$Q= \int_0^\infty I_{abs}(q)\, q^2\, dq = 2\pi^2 \left\langle \eta^2 \right\rangle \qquad\qquad /6/$$

where $I_{abs}(q)$ is the absolute scattered intensity per unit volume, equal to the experimental intensity divided by the sample thickness, and $<\eta^2>$ is the average fluctuation of the density of scattering length within the irradiated volume[1].

At early times (6 min), the matrix elements E10 to E7 are well matched by the scattered intensity of BSA and their relative concentrations are 1.04, 1.12, 1.25 and 2.5 times that of the BSA solution. Accordingly, the concentration of aggregates that have accumulated in matrix element is respectively 0.04, 0.12, 0.25 and 1.5 times that of the BSA solution (Table SI-1). The spectra from matrix elements E6 to E3 cannot be matched by the spectrum of BSA, because they contain essentially the scattered intensity from the ACH polycations.
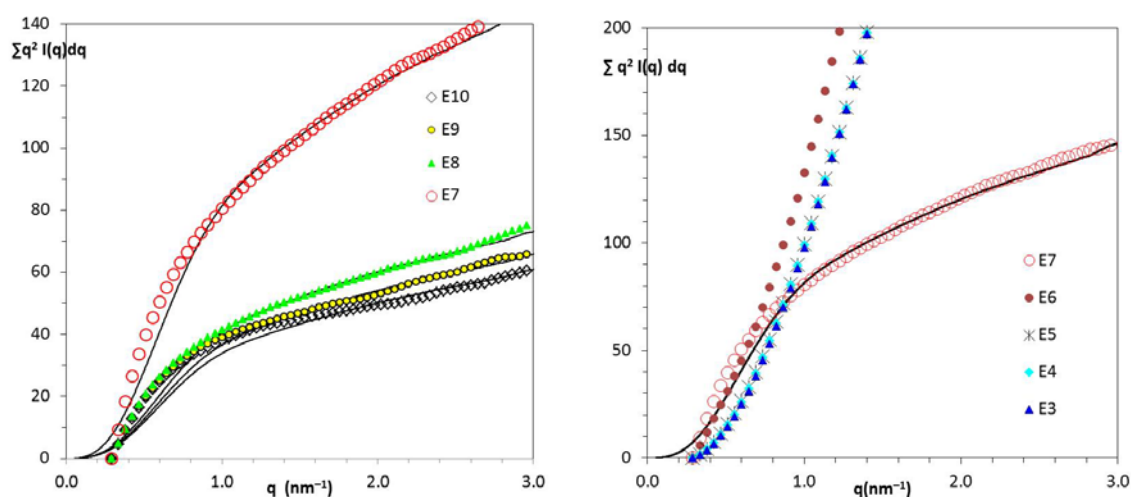

Figure SI-2: Calculation of the concentration of solutes in each cell at short time t = 6 min. For each scattering image, the symbols are the data and the full line is the spectrum of the BSA solution scaled to match that of each cell. Vertical: values of the integral of the scattering over all directions of reciprocal space, $\sum q^2 I(q)dq$ (arbitrary units). The high-q limit of this integral is proportional to the average concentration of the solute molecules[1]. Horizontal: values of scattering vector q.

At late times (Fig. SI-3), the cells E10 to E6 are well matched by that of BSA and their relative concentrations are 2.9, 3.5, 3.8, 4.8 and 29 times that of the BSA solution (Table SI-1). Accordingly, the concentration of aggregates that have accumulated in each cell is respectively 1.9, 2.5, 2.75, 3.8 and 28 times that of the BSA solution. The spectra from cells E5 to E3 cannot be matched by that of BSA, because they contain mostly the scattering from the ACH polycations.

---

[1] A. Guinier and G. Fournet, Small Angle Scattering of X-rays, Wiley 1955; O. Glatter and O.Kratky, Small Angle X-ray Scattering, Academic Press 1982; P. Lindner and Th. Zemb, Neutron, X-rays and Light: Scattering Methods Applied to Soft Condensed Matter, North Holland 1982
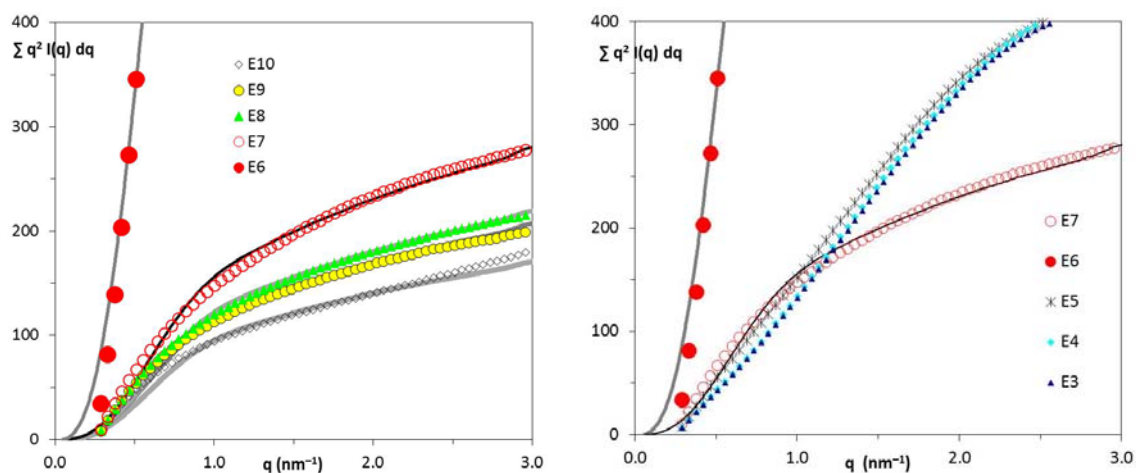
Figure SI-3: Calculation of the concentration of solutes in each cell at long time t = 32 min. For each scattering image, the symbols are the data and the full line is the spectrum of the BSA solution scaled to match that of each cell. Vertical: values of the integral of the scattering over all directions of reciprocal space, $\sum q^2 I(q)dq$ (arbitrary units). The high-q limit of this integral is proportional to the average concentration of the solute molecules[1]. Horizontal: values of scattering vector q.

Cell number	Scaling factor at 6 min	Scaling factor at 32 min
E10	0.04	1.9
E9	0.12	2.5
E8	0.25	2.8
E7	1.5	3.8
E6	-	28

Table SI-1: values of the scaling factors obtained by matching integral of the scattering with that of BSA.

We explored these phenomena further by measuring the intensity along a horizontal line (6th line from top). These measurements are presented in Fig. SI-4. They show the transfer of « lumps » of scattering material along the line, first to the front of the line (t=18 to 20 min), then to the rear (t = 22 to 24 min), then back to the center (t = 26-32 min). These displacements of large amount of connected material across the junction appear to precede the onset of faster accumulation kinetics (see the increase in accumulation rate that takes place after the displacement at t = 20-24 min). We interpret these phenomena by assuming that hydrodynamic forces push small pieces of gel into locations where they effectively plug the flow and lead to a faster accumulation of proteins into the plug.
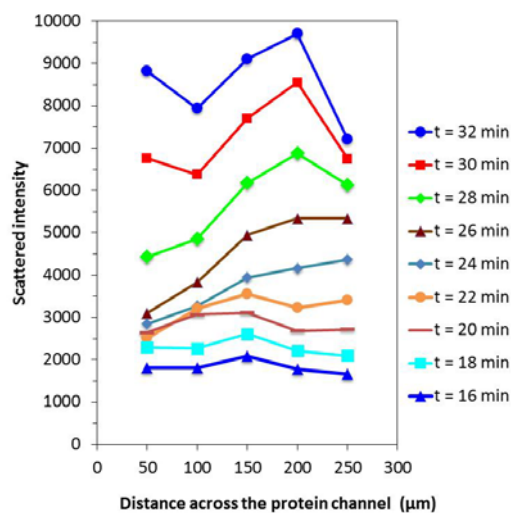
Figure SI-4: Profiles of intensity scattered at low q values by cells located along a horizontal line (6th line from top).

Figure SI-5 shows the impact of structural parameters on scattering intensity fit, in complement to Figure 5 (scattering intensities from the separated components of the system). In order to give an idea of the precision in the determination of the mass per polycation, we have changed the fit parameters for the ACH spectrum showing spectra for 19, 25 or 33 Al atoms.
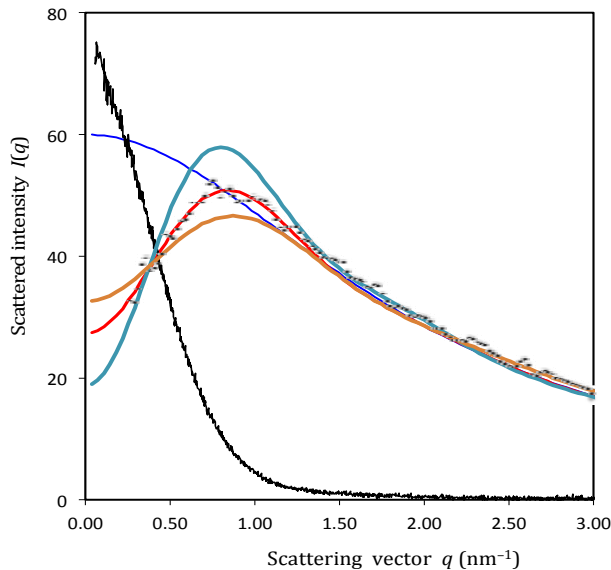

Figure SI-5: SAXS spectra from both solutes ACH and BSA, each one alone in water. Full black line: spectrum from a 1% BSA solution. Black dots: spectrum from a 1% ACH solution. Blue line: model for repelling branched ACH polymers containing 33 Al atoms. Full red line (same as in Fig. 5): model for 25 Al atoms. Orange line: model for 19 Al atoms. Structural parameters used to fit the scattering intensity plot: volume fraction ACH = 0.068, fractal dimension ACH = 2.1, gyration radius ACH = 0.9 nm, repulsion length = 5.5 nm, ACH scale factor = 60.

Figure SI-6 presents the scattered intensity measured along the central column at long times, shortly after plug expulsion. The SAXS spectra can then be decomposed into a contribution from free proteins and another one from free polycations. The fits are the interdiffusion profiles of polycations into the protein solution and of proteins into the polycation solution, calculated from Fick's law for one-dimensional diffusion of a solute from a fixed boundary.
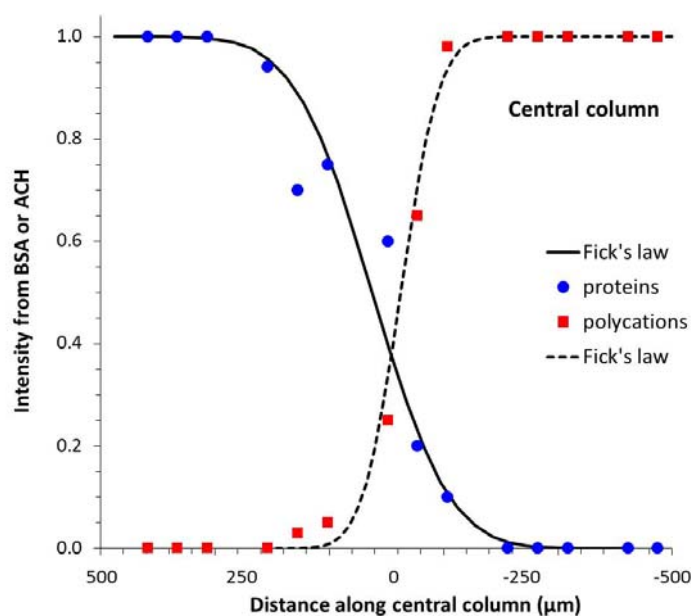

Figure SI-6: Relative intensities scattered at very long times by cells along the central column. The intensity scattered by each cell can be decomposed into a contribution from BSA (dark blue dots) and a contribution from free ACH (red dots).

3) Movies M1.wmv M2.avi

a**)** Supplementary **Movie M1** associated to **Fig. 3**.

Typical aggregation patterns observed with microfluidic chip flowed by 0.1 nL.s^{-1} natural eccrine sweat and 1 nL.s^{-1} aqueous 15% ACH in surface channel, corresponding to Figure 3 conditions (sweat channel width = 50 µm). Video rate: one image every minute.

b) Supplementary **Movie M2** associated to **Fig. 4**.

Typical aggregation patterns observed with V2 microfluidic chip flowed by 0.5 nL.s^{-1} artificial sweat containing 0.1% BSA (15 µM) and 1 nL.s^{-1} aqueous 15% ACH in "surface channel", corresponding to Figure 4 conditions (channel width 300 µm). Video rate: one image every 15 s.